Modelling and experimental study on β-phase depletion behaviour of HVOF sprayed free-standing CoNiCrAlY coatings during oxidation

H. Chen[a,*], G. A. Jackson[b], K. T. Voisey[b] and D. G. McCartney[b]

[a]Department of Mechanical, Materials and Manufacturing Engineering, Faculty of Science and Engineering, University of Nottingham Ningbo China, Ningbo 315100, China

[b]Advanced Materials Research Group, Faculty of Engineering, University of Nottingham, University Park, Nottingham NG7 2RD, UK

Abstract

This paper investigates the β-phase depletion behaviour during oxidation of free-standing CoNiCrAlY (Co-31.7%Ni-20.8%Cr-8.1%Al-0.5%Y, all in wt%) bond coats prepared by high velocity oxy-fuel (HVOF) thermal spraying. The microstructure of the coatings was characterised using scanning electron microscopy with energy dispersive X-ray (EDX) analysis and electron backscatter diffraction (EBSD). It comprises a two phase structure of fcc γ-Ni and bcc β-NiAl, with grain sizes varying largely from 0.5 to 2 μm for both phases. Isothermal oxidation tests of the free-standing coatings were carried out at 1100 °C for times up to 250 h. The β phase depletion behaviour at the surface was measured and was also simulated using Thermo-Calc and DICTRA software. An Al flux function derived from an oxide growth model was employed as the boundary condition in the diffusion model. The diffusion calculations were performed using the TTNi7 thermodynamic database together with the MOB2 mobility database. Reasonable agreement was achieved between the measured and the predicted element concentration and phase fraction profiles after various

time periods. Grain boundary diffusion is likely to be important to element diffusion in this HVOF sprayed CoNiCrAlY coating due to the sub-micron grains.

*Corresponding Author. Tel.: +86-574-88180946; Fax: +86-574-88187462.

E-mail address: Hao.Chen@nottingham.edu.cn

1.   Introduction

Thermal barrier coatings (TBCs) are widely used to protect high temperature components in turbine engines from harsh operating environments [1, 2]. TBC systems consist of a ceramic top coat, a metallic bond coat and a superalloy substrate [3-5]. Additionally, a thermally grown oxide (TGO) forms at the interface between the top coat and the bond coat during service at elevated temperature due to the fact that oxygen permeates through the ceramic top coat and oxidises the bond coat. The durability of the overall TBC system is largely determined by the microstructural, chemical and mechanical characteristics of the bond coat [6-8]. Among different types of bond coats, MCrAlY overlay coatings, where M = Co, Ni or a combination of the two, are of great interest for their excellent oxidation resistance and good adhesion between the top coat and the superalloy substrate [9-16]. Depending on the compositions, MCrAlYs generally exhibit a multi-phase structure; e.g. a fcc γ-Ni matrix and a bcc β-NiAl secondary phase. The β-NiAl acts as an aluminium source and promotes the stable and continuous formation of aluminium oxides, predominantly Al_2O_3, during oxidation. This Al_2O_3 scale, also referred to as the TGO, forms between the top coat and the MCrAlY bond coat [10, 17-19]. It is widely recognised that the growth of the TGO during service causes progressive build-up of stress in the system, leading to the spallation of the ceramic top coat and eventually causing detrimental effects to the turbine engine components [20-22]. The continuous growth of the TGO due to aluminium diffusion from the MCrAlY bond coat results in subsequent β phase depletion at the oxide/bond coat interface [23-28], causing mechanical and chemical degradation of the coating. Degradation of the bond coat also occurs due to interdiffusion of element between the MCrAlY and the superalloy substrate. This is not considered in the present paper but has been studied by others, e.g. [29-41]. In these research works, the emphasis has been on substrate/bond coat interdiffusion and specific comparisons between measured and predicted β-phase depletion at the oxide/bond coat interface have not been considered. On the other hand, several analytical models concerned with the oxidation of

two phase systems in which the secondary phase dissolves during oxidation have been reported, e.g. [42-48]. In these models, the secondary phase depletion behaviour during oxidation can generally be represented by the parabolic diffusion law, Eq. (1),

$$x_d \sim \sqrt{t} \qquad (1)$$

where x_d is the width of the second phase depletion zone and t is the oxidation time.

Considering the significance of β depletion on the degradation of TBCs, therefore, the aims of the work reported in this paper were to investigate specifically the kinetics of β depletion at the oxide surface in free-standing MCrAlY coatings during isothermal oxidation, to develop a numerical model for phase evolution and element diffusion using the available thermodynamic and kinetic data of the MCrAlY system, and to study the grain size effect in these thermally sprayed MCrAlY coatings.

2. Materials and experimental procedure

2.1 Materials preparation, heat treatment and isothermal oxidation

The coatings used for isothermal oxidation experiments were prepared by high velocity oxy-fuel (HVOF) thermal spraying using powder with a nominal composition of Co-31.7%Ni-20.8%Cr-8.1Al%-0.5%Y (all in wt%). The powder was obtained from Praxair (commercially available as CO-210-24) and had a size range -45+20 μm. The coatings were deposited onto 800-grit ground mild steel substrates with dimensions $60 \times 25 \times 1.8$ mm using a Met Jet III liquid fuel HVOF gun. The details of the spraying process are given in reference [49]. Coatings were sprayed to a thickness of approximately 0.5 mm and were then debonded from the ground substrate by bending around a mandrel. Two surface conditions were used in the experiments on the debonded free-standing CoNiCrAlY coatings: (I) an as-sprayed rough surface (surface roughness, $R_a = 6.1 \pm 0.5$ μm) and (II) a polished surface ($R_a = 0.2 \pm 0.1$ μm).

An initial vacuum heat treatment (HT) was given to the debonded coatings prior to oxidation. Coatings were heat treated in a vacuum with a nominal pressure of 6.0×10^{-3} mbar at 1100 °C for 2 h followed by air cooling to replicate the initial heat treatment given to the bond coat material in conventional TBC manufacture. Previous work has demonstrated that the initial heat treatment has the effect of reducing any coating porosity to a minimal level [49] and allows the β phase to coarsen and precipitate [50]. For isothermal oxidation experiments, heat treated samples were exposed to laboratory air in a Carbolite furnace at 1100 °C for 50 h, 75 h, 100 h and 250 h followed by natural air cooling.

2.2   *Material characterisation*

For microstructural observations, samples were mounted in a conductive resin and successively ground and polished to a 1 μm surface finish. The microstructures of coating cross-sections before and after isothermal oxidation were examined in a FEI XL 30 scanning electron microscope (SEM) operated at 20 kV. Backscattered electron (BSE) imaging was used to form images and semi-quantitative energy dispersive X-ray (EDX) analysis was also utilised to obtain element profile measurements and phase identification through chemical analysis. Image analysis software, ImageJ [51], was used to measure the width of the β depletion zone and β-phase volume fractions. SEM-based electron backscatter diffraction (EBSD) was carried out to investigate the grain morphology of coating cross-sections using a Zeiss 1530 VP field emission gun scanning electron microscope (Carl Zeiss, Inc, Mape, Grove, MN) with an EDAX Pegasus combined electron backscatter diffraction system (EDAX, Mahwah, NJ, USA). For EBSD analysis, a further stage of chemical/mechanical polishing using colloidal silica was required after the standard grinding and polishing procedure to achieve reduced surface deformation. The EBSD patterns were recorded at an acceleration voltage of 20 kV with a beam current of 26 nA at a specimen tilt angle of 70°.

EBSD maps were collected with a step size of 0.1 μm and areas of 50 μm × 50 μm. The EBSD data acquisition and processing were performed using the EDAX OIM5 software suite.

3.   Modelling procedure

3.1   Model description

The initial composition is taken to be Co-31.7Ni-20.8Cr-8.1Al (all in wt%). The small amount (~0.5 wt%) of Y actually present in the alloy is neglected and remaining elements are scaled accordingly. The alloy is assumed to be at thermodynamic equilibrium initially and the temperature is set to be 1100 °C. The free-standing coating is held at this temperature for different periods of time and Al_2O_3 growth, taken to be planar, occurs on both surfaces according to a kinetic law (described later in section 3.2). At any time, t, the microstructure during oxidation is shown by the schematic cross-section of Fig. 1. In this system, the Al_2O_3 scale grows at the oxide/coating interface and is in contact with a single γ-Ni phase region known as the β depletion zone whilst the interior of the sample comprises a two phase (γ + β) region as predicted by thermodynamic equilibrium for the alloy composition. During oxidation, the β phase volume fraction is expected to vary as shown schematically in Fig. 2, where the β phase depletes as the Al_2O_3 forms and eventually the fraction of β in the γ+β region decreases.

3.2   Oxidation model

The β depletion model assumes that growth of Al_2O_3 scale requires a flux of aluminium from the coating. Owing to the approximately planar nature of this free-standing coating system, the whole system can be approached by a one-dimensional model. In this study, the oxidation model reported by Meier et al. [34] for a Ni-Co-Cr based bond coat was employed, in which they proposed a simplified power law oxide growth model as expressed in Eq. (2),

6

$$\delta_{(\mu m)} = \left\{ exp\left[Q\left(\frac{1}{T_0} - \frac{1}{T}\right)\right] t \right\}^n \qquad (2)$$

where $Q = \Delta H/R$, ΔH is the activation energy in J/mol, R is the gas constant in J/(mol·K). T_0 is a temperature constant in K, T is the oxidation temperature in K, t is the oxidation time in seconds and n is a constant. By the combination of the above parameters, oxide growth thickness can be obtained in μm. Q, T_0 and n were found by Meier et al. to be 27777.4 K, 2423.7 K and 0.332 respectively by fitting this oxide growth behaviour between 1038~1149 ℃ to experimental data [34]. Taking a differential of Eq. (2) with respect to time, the oxide growth rate can be obtained as Eq. (3).

$$\dot{\delta}_{(\mu m/s)} = n\left\{ exp\left[Q\left(\frac{1}{T_0} - \frac{1}{T}\right)\right] t \right\}^{n-1} \qquad (3)$$

Following the approach implemented by Nesbitt et al. [30], the Al flux, J_{Al}, at the oxide/coating interface can be determined by Eq. (4), which is used as the boundary condition in the DICTRA diffusion model in the following section,

$$J_{Al} = \dot{\delta} \cdot \rho_{ox} \cdot r \qquad (4)$$

where $\dot{\delta}$ is the oxide growth rate, ρ_{ox} is the density of the oxide, taken as the density of Al_2O_3 in this study (3950 kg/m^3), r is the ratio of the atomic weight of Al to Al_2O_3. Oxidation will cause the material surface to recede due to the continuous loss of elements in the material. However, according to the nature of the alumina growth [52], the surface recession is very small, this has also been demonstrated by Nesbitt et al. [30]. Thus in the current work, surface recession is neglected.

3.3   Diffusion modelling

Initial phase fraction calculations were carried out using Thermo-Calc [53] and diffusion modelling was performed using finite difference software DICTRA from Thermocalc-AB

[54]. The diffusion modelling is based on Fick's first law, Eq. (5), and Fick's second law, Eq. (6),

$$J_k = -D_k \cdot \frac{\partial C_k}{\partial x} \tag{5}$$

$$\frac{\partial C_k}{\partial t} = \frac{\partial}{\partial x}(-J_k) = \frac{\partial}{\partial x}\left(D_k \cdot \frac{\partial C_k}{\partial x}\right) \tag{6}$$

where, J_k is the interdiffusion flux of element k, C_k is the concentration of k and D_k is the interdiffusion coefficient of element k. DICTRA alternatively uses the chemical potentials and mobility of the individual elements to extend Fick's first law, which can be expressed as Eq. (7),

$$J_k = -\sum_{i=1}^{n} L'_{ki} \cdot \sum_{j=1}^{n} \frac{\partial \mu_i}{\partial C_j} \cdot \frac{\partial C_j}{\partial x} \tag{7}$$

where μ_i are the chemical potentials of elements and $\partial \mu_i / \partial C_j$ are purely thermodynamic quantities. The term L'_{ki} can be considered as the proportionality factor which depends on the mobility of the individual elements. Therefore, by combining Eq. (6) and (7), numerical solutions can be achieved through finite difference methods if thermodynamic data and mobility data are available. More details about DICTRA software are given in reference [54]. In this study, thermodynamic data were obtained from the nickel superalloy database, TTNi7, supplied by Thermotech [55] and mobility data were obtained from the kinetic mobility database, MOB2, supplied by Thermo-Calc.

3.3.1 Initial conditions

Considering the symmetry boundary of the coating oxidation system shown in Fig. 2, the width of the model is set to 250 μm, i.e. half the thickness of the debonded coating. The schematic diagram of the model is shown in Fig. 3, where the boundary condition at the oxide/coating interface is the Al flux and the other side of the model is set as a closed system

with zero flux boundary. In the majority of the calculations, a grid was used where, in the first 50 μm from the oxide/coating interface, the grid spacing is kept at 0.2 μm and then in the remaining 200 μm the grid spacing is set to 2 μm. The elements considered are Al, Ni, Co, and Cr and the phases considered are γ-fcc and β-NiAl, where β-NiAl phase is defined as a dispersed phase of equilibrium composition.

Since the coatings received an initial heat treatment at 1100 °C for 2 h, an initial oxide, associated with an initial β depletion zone, formed at the coating surface. By assuming this initial oxide is in the form of Al_2O_3 and assuming the Al used to form this initial Al_2O_3 layer is all sourced from the β phase, the corresponding initial β depletion zone can be estimated with respect to the initial oxide thickness through a mass balance conversion. This is summarised in Table 1 for three different assumed initial oxide thicknesses. In this study, an initial oxide of 1 μm associated with a 5.6 μm initial β depletion zone was selected to account for the initial experimentally observed β depletion zone of about 5 μm formed after the initial heat treatment at 1100 ℃ for 2 h. The initial element concentration profiles are given as step profiles where the element composition in the initial β depletion zone is taken as the γ phase composition, calculated from Thermo-Calc (Table 2) at 1100 ℃, and the composition in the γ+β region is taken as the initial alloy composition (Co-31.7%Ni-20.8Cr-8.1%Al-0.5%Y, all in wt%) by normalising the elements to 100% excluding Y. This initial step profile is shown in Fig. 4. The effects of different initial oxide thicknesses on the growth of β depletion zone are investigated and discussed in Section 5.2.

3.3.2 Boundary conditions

As described earlier, an Al flux function (Eq. (4)) derived from the oxide growth model (Eq. (2)) was obtained. To avoid an infinite Al flux at the beginning of the diffusion calculations, it was assumed that 1 μm Al_2O_3 had already formed before the diffusion

calculation started. This was to account for the initial β depletion zone of about 5 μm which formed after the initial heat treatment at 1100 ℃ for 2 h. Thus the initial aluminium flux is taken as the flux value after 1 μm oxide has formed, where t^1 is the time for the oxide to reach 1 μm. t^1 can be obtained from Eq. (2), for 1 μm oxide, $t^1 = 6441 s$. Subsequently the flux of Al, J_{Al}, follows Eq. (4) in the diffusion calculations.

3.3.3 Labyrinth factor

The standard DICTRA model considers diffusion only in the γ matrix while the secondary phases like β-NiAl are held as non-diffusional phases [54]. Diffusion through the dispersed phase (the β phase in the present model) is neglected, but its effect on diffusion in the matrix by reducing the area available for diffusion (i.e. blocking the diffusion paths) is incorporated via a labyrinth factor which depends on the volume fraction and geometry of the precipitates. The β-NiAl phase is defined as a dispersed phase that acts as point sinks or sources, the fractions of which grow or shrink depending on the simulated composition at each location. This impeding effect of dispersed phases on diffusion is accommodated by a so-called labyrinth factor, represented as a function of the volume fraction of the dispersed phases. Following a similar approach used by Hashin and Shtrikman [56], Gomez-Acebo et al. [57] proposed the upper and lower bounds for effective diffusivity in a two-phase material, can be given as,

$$D_{eff}^{upper} = D_\gamma + \frac{f_\beta}{1/(D_\beta - D_\gamma) + f_\gamma/(3D_\gamma)} \qquad (8)$$

$$D_{eff}^{lower} = D_\beta + \frac{f_\gamma}{1/(D_\gamma - D_\beta) + f_\beta/(3D_\beta)} \qquad (9)$$

where, D_β and D_γ are the diffusivities for β and γ respectively. Taking the diffusion data from the work reported by Karunaratne et al. [33], $D_\beta \approx 0.1D_\gamma$, the above bounds can be rewritten as:

$$D_{eff}^{upper} = D_\gamma \cdot (1 + \frac{3 - 3f_\gamma}{f_\gamma - \frac{10}{3}}) \qquad (10)$$

$$D_{eff}^{lower} = D_\gamma \cdot (0.1 + \frac{0.9f_\gamma}{4 - 3f_\gamma}) \qquad (11)$$

The terms in brackets are the labyrinth factor. In this study, the upper bound was used in the DICTRA calculations. It has to be emphasised that this may not be the upper bound for diffusion in the actual system, but only as a first approximation. After the above conditions were set, diffusion calculations were performed at 1100 °C for 250 h at a time step of 1000 s using a fully implicit solution method.

4. Results

4.1 Microstructural analysis

Typical SEM micrographs of the HVOF sprayed CoNiCrAlY bond coat after heat treatment are shown in Fig. 5, where Fig. 5(a&b) are the coating with a rough surface and a polished surface respectively. It can be seen an initial alumina layer and an initial β depletion zone have developed at the coating surface. This initial β depletion zone is an average of ~5 μm. Fig. 5(c) shows a dual phase structure of the CoNiCrAlY bond coat, in which the brighter phase is the fcc γ matrix and the darker phase is the bcc β secondary phase. Oxide stringers that formed due to HVOF spraying can also be found in the coating as shown in Fig. 5(c). The volume fraction of the β phase is 30% ± 2% as measured by image analysis. A plot of phase mass fraction versus temperature obtained from Thermo-Calc is presented in Fig. 6 using the TTNi7 thermodynamic database. It can be seen that the expected constitution at 1100 °C is

γ+β. The mass fractions of the γ and β phase obtained from Thermo-Calc are converted to volume fraction using an approach stated in reference [7] and these agree well with experimentally measured volume fractions, as summarised in Table 3 assuming phase equilibrium at 1100 °C. The composition of each phase was measured by EDX and summarised in Table 2. It can be seen that the experimentally measured phase compositions generally agree with those obtained from the TTNi7 database at 1100 °C. It is worth noting that the measured Ni and Cr contents in the γ phase are larger than the calculated contents whilst Co is slightly lower compared to the value from the database. The inverse pole figure map and phase distribution map derived from EBSD data are shown in Fig. 7(a) and Fig. 7(b) respectively. These figures reveal that the β-phase dimensions are typically 0.8~2 μm and appear to be largely monocrystalline. The γ phase is clearly polycrystalline with approximately equiaxed grains that exhibit a wide range of grain diameters typically from 2 μm to 500 nm or less. Many of the γ grains are twinned but there is no evidence for preferred orientation in either γ or β phases.

4.2   β depletion during isothermal oxidation

After isothermal oxidation at 1100 °C, an alumina scale has formed on the coating surface, resulting in the β depletion zone formation, typically shown in Fig. 8. The β depletion zone grows progressively with the oxidation time. The β depletion zone measurements were carried out from the edges of β phase particles to the coating surface and are plotted in Fig. 9, including the initial β depletion zone after heat treatment. It can be seen that the β depletion zone at the rough surface is about 2 times larger than that at the polished surface. An EBSD map of the microstructure in the region of the β depletion zone after 250 h oxidation is shown in Fig. 10. It can be seen that both the γ and β grains have coarsened due to annealing at 1100 °C (compare with Fig. 7). The γ phase remains twinned with polycrystalline equiaxed grains and no preferred orientation has developed for either phase.

4.3   Modelling results

Fig. 11 shows the phase fraction evolution obtained from DICTRA calculations for periods of

50 h, 75 h, 100 h and 250 h at 1100 °C. The initial β depletion zone, which resulted from the

initial step element profile defined previously in Fig. 4, is also included in this figure. It can

be seen that the β phase depletes from the surface as time increases. Typical element

composition profiles after 100 h simulation are shown in Fig. 12. It can be seen that the Al

content is about 4.8 wt% at the oxide/coating interface. Concentrations of the other elements

change as a result of diffusion which is driven by the chemical potential gradients in the alloy.

Since the Al loss is crucial to the β depletion, Al concentrations in the coating over different

time periods are plotted in Fig. 13. It can be observed that the Al content in the β depletion

zone is calculated to be ~4.8 wt%, and increases to an average of 8.1 wt% in the γ+β region

for times up to 100 h. For 250 h, the Al content in the γ+β region decreases below 8.1 wt%

due to the continuous loss of Al causing the overall β fraction in the γ+β region to decrease

slightly. It is worth noting that the Al concentration gradient in the β depletion zone is shallow

but the mobility of the Al is high.

The element composition profile after 250 h oxidation at 1100 °C determined by EDX

analysis is compared to the modelling results in Fig. 14. Although larger β depletion is

predicted in the modelling data, the element concentrations are in good agreement with the

model predictions. It can be seen that the measured Al concentration in the β depletion zone

fluctuate between 4.6~4.8 wt%. Ni and Cr have a slightly larger concentration while Co

shows a smaller concentration compared to the model predictions. Since the Al loss is

determined by the Al flux (which is derived from the oxide growth model, Eq. (2)), the actual

value of Al flux is closely related to the assumed initial oxide thickness. Thus, the β depletion

zone develops at different rates according to this assumption in Fig. 15. Since the oxide

growth model is based on a power law with a growth exponent of 0.332, the β depletion may not strictly exhibit the parabolic oxidation but in this case it is nearly parabolic, as shown in Fig. 15.

5. Discussion

5.1 Surface roughness

The β depletion zone can be employed to help interpret the oxidation behaviour of CoNiCrAlY coatings in an indirect way. Since the oxide layer may spall off during oxidation or sample preparation, β depletion can be a representative way to interpret oxidation. It is shown in Fig. 9 that the β depletion zone in samples with a rough oxidising surface is greater than in samples with a polished surface. The larger surface contact area will result in a greater Al flow and lead to more severe β depletion, especially in those regions that are convex. Consequently, larger β depletion zones are formed at a rough surface compared to a polished surface. This agrees with other work reported in the literature [12, 19, 58]. It has also been reported that surface roughness can affect the yttrium distribution by forming yttrium aluminides in concave regions of the coating [59], but this has not been observed in this study.

5.2 Effects of initial oxide thickness

In TBC applications, pre-heat treatment is frequently utilised to produce a thin alumina scale on the bond coat surface. It is widely believed that this pre-existing alumina scale can stimulate further alumina growth. To model this condition, an initial oxide associated with an initial β depletion zone was assumed. Since the Al flux is derived from the oxide growth model, it will be infinite at the boundary unless a finite initial oxide thickness is applied. As a result of the presence of the initial oxide, the Al flux has a finite starting value, depending on the thickness assumed. When the diffusion calculation starts, for a 1 μm initial oxide thickness, compared to the other two conditions, the initial Al flux is one order of magnitude

14

smaller. Therefore, in Fig. 15, the β depletion rate for an initial 1 μm oxide is slower. Since the β phase is defined as a dispersed phase in the DICTRA model, the β-phase fraction decreases to supply the Al to the oxide. The continuous loss of Al causes the β phase to deplete progressively. For a thinner initial oxide thickness with higher Al flux, the β depletion occurs more rapidly. In Fig. 15, it can also be seen that with different initial oxide thicknesses, β depletion still exhibits nearly parabolic growth behaviour.

5.3   Comparison between modelling and experimental results

Since Meier's model [34] for oxide growth was developed for a rough surface, the comparison between the EDX composition measurements and modelling results is carried out for the rough surface samples in Fig. 14. The offsets of Co, Ni and Cr in Fig. 14 may be attributed to the intrinsic compositional difference between the measured and calculated phase compositions. It is indicated in Table 2 that the measured Ni and Cr contents are larger than the calculated contents in the γ phase whilst Co is lower. In DICTRA diffusion calculations, the main driving force for the element concentration evolution is due to the chemical potential difference of each element and it partially depends on the concentration of other elements. Since Al flux is the only boundary condition in this model, changes in the concentration of Co, Ni and Cr are only driven by the chemical potential of each element. As such, a new element profile is developed after Al flux is applied. Therefore, the pre-existing discrepancy between the calculated and measured phase compositions could still be retained. Some offsets of the element profiles are observed, nevertheless they show reasonably satisfying agreement. It is also worth noting that, in reality, the oxidation is a very complicated process, involving the formation and spallation different oxides, such as spinel oxides $((Ni,Co)(Al,Cr)_2O_4)$. This may create further discrepancy between the experimental measurements and the modelling predictions.

The experimentally measured β depletion zone thickness at the rough surface of the free-standing CoNiCrAlY coating is compared to the modelling results as plotted in Fig. 16. The modelling predictions that assume a 1 μm initial oxide thickness are used to compare with experimental β depletion measurements as this initial oxide thickness is typical of what is found experimentally. It can be seen that the predicted β depletion zone widths are slightly larger than the measured ones. This might be attributed to several factors. Firstly, the impeding effects from the dispersed β phase may not be properly accounted for by the labyrinth factor in the DICTRA software, in which case the effective diffusivity within the γ matrix is too high. This could result in larger β depletion zone width in the calculations. Secondly, the oxide growth model has already been demonstrated to have a significant effect on the β depletion calculations since the boundary condition, Al flux, is based on the oxide growth model. It is indicated in Eq. (2) that the Al flux is very large at the beginning of oxidation, which agrees well with the classic oxidation modelling where the initial flux at the boundary is nearly infinite [60]. Though the assumed β depletion zone is similar to that formed after the initial heat treatment, the resultant Al flux after an initial oxide has been applied may still be too large. But it is worth noting that modelling data in Fig. 16 show a good fit with the parabolic diffusion law, as described in Eq. (1).

5.4   Element diffusion mechanism

It can be seen in Fig. 14 that the Al concentration gradient in the β depletion zone is very shallow. This concentration gradient of Al in the depletion zone is determined by two factors namely the chemical potential gradient and the mobility or diffusion coefficient of Al. In modelling, using DICTRA as well as other relevant work published in the literature, diffusion is only considered to be lattice diffusion. However, in the case of a very fine grain structure, as is shown to exist in Fig. 7, grain boundary diffusion may have also contributed.

In a fine grained material, the grain boundary area is much greater than the cross-sectional area. Therefore, atoms, such as Al, diffusing along the grain boundaries will be able to diffuse much faster than atoms diffusing through the lattice. In other words, the grain boundary offers an easy element diffusion path, which eventually affects the apparent diffusion coefficient as expressed in Eq. (12) [61],

$$D_{app} = D_l + D_b \cdot (\Delta/d) \tag{12}$$

where D_l is the lattice diffusion coefficient and D_b is the grain boundary coefficient, Δ is the width of the grain boundary, normally taken as ~0.5 nm, and d is the grain size, taken as 1 μm in our case. The activation energy for diffusion along the grain boundary (Q_b) is lower than that for lattice diffusion (Q_l) and it is generally found in fcc metals that $Q_b \sim 0.5\ Q_l$. Taking the diffusion data from the work reported by Karunaratne et al. [33], by applying the parameter in Eq. (12), the apparent diffusion coefficient can be obtained as shown in Fig. 17 as a function of temperature. It can be seen that at 1100 °C, both lattice diffusion and grain boundary diffusion contribute to the apparent diffusion coefficient due to a very fine grain size. The apparent diffusion coefficient for Al is larger than the lattice diffusion coefficient. However, the experimentally measured β depletion zone widths are smaller than the model predictions in Fig. 16 and so it is possible that the Al flux derived from the oxide growth model is too large and leads to more severe β depletion in the diffusion calculations. Similar observations have been found in work reported by Karunaratne et al. [33] in that the β depletes at a faster rate in their model compared to their experimental β depletion. Future work is required to develop a more suitable oxide growth model and account for the grain boundary diffusion for specific CoNiCrAlY coatings to produce more reliable predictions.

6.   **Conclusions**

- Microstructural characterisation reveals a very fine grain structure in the HVOF sprayed CoNiCrAlY bond coat, with a twinned γ grain structure at a grain size varying largely between 0.5~2 μm and a monocrystalline structure of β phase with a grain size of about 0.8~2 μm

- It is found that a rough oxidising surface results in a larger β depletion zone compared to a polished smooth surface due to a larger surface area of the rough surface.

- A numerical model employing the Thermo-Calc and DICTRA software gives reasonably good agreement with the experimental observations in both β depletion zone growth and element concentration profiles by using an Al flux function as the boundary condition. It is assumed that a 1 μm oxide has already formed after the initial heat treatment. The Al flux function is derived from the oxide growth equation of Meier et al. [34].

- Further work on improving the oxide growth model and effective diffusion coefficients within the MCrAlY will be necessary to improve agreement between model predictions and experimental measurements.

7.   Acknowledgements

8.   References

[1] G.W. Goward, Surf. Coat. Technol., 108–109 (1998) 73-79.
[2] J.R. Nicholls, JOM, 52 (2000) 28-35.
[3] J.R. Nicholls, K.J. Lawson, D.S. Rickerby, P. Morrell, AGARD Report 823 "Thermal Barrier Coatings" (1998).
[4] A.G. Evans, D.R. Mumm, J.W. Hutchinson, G.H. Meier, F.S. Pettit, Prog. Mater Sci., 46 (2001) 505-553.
[5] D. Stöver, C. Funke, J. Mater. Process. Technol., 92-93 (1999) 195-202.
[6] H. Chen, T.H. Hyde, K.T. Voisey, D.G. McCartney, Mater. Sci. Eng., A, 585 (2013) 205-213.

[7] H. Chen, Ph.D Thesis, Department of Mechanical, Materials and Manufacturing Engineering, University of Nottingham, (2015).

[8] H. Chen, T.H. Hyde, K.T. Voisey, D.G. McCartney, Proc IMechE Part L: J Materials: Design and Application, DOI 10.1177/1464420715622495 (2016).

[9] W. Quaddakers, A. Tyagi, D. Clemens, R. Anton, L. Singheiser, Elevated temperature coatings: Science and technology III, (1999) 119-130.

[10] J. Toscano, R. Vaen, A. Gil, M. Subanovic, D. Naumenko, L. Singheiser, W.J. Quadakkers, Surf. Coat. Technol., 201 (2006) 3906-3910.

[11] R.D. Jackson, Ph.D thesis, University of Birmingham, University of Birmingham, (2010).

[12] A. Gil, V. Shemet, R. Vassen, M. Subanovic, J. Toscano, D. Naumenko, L. Singheiser, W.J. Quadakkers, Surf. Coat. Technol., 201 (2006) 3824-3828.

[13] S. Saeidi, K.T. Voisey, D.G. McCartney, J. Therm. Spray Technol., 18 (2009) 209-216.

[14] C.S. Richard, G. Béranger, J. Lu, J.F. Flavenot, Surf. Coat. Technol., 82 (1996) 99-109.

[15] M. Okazaki, S. Yamagishi, Y. Yamazaki, K. Ogawa, H. Waki, M. Arai, Int. J. Fatigue, 53 (2013) 33-39.

[16] H. Chen, D.G. McCartney, K.T. Voisey, Mater. High Temp., 32 (2015) 215-220.

[17] W. Brandl, D. Toma, H. Grabke, Surf. Coat. Technol., 108 (1998) 10-15.

[18] P. Puetz, X. Huang, R.S. Lima, Q. Yang, L. Zhao, Surf. Coat. Technol., 205 (2010) 647-657.

[19] J. Toscano, D. Naumenko, A. Gil, L. Singheiser, W.J. Quadakkers, Mater. Corros., 59 (2008) 501-507.

[20] E.A.G. Shillington, D.R. Clarke, Acta Mater., 47 (1999) 1297-1305.

[21] Y.H. Sohn, J.H. Kim, E.H. Jordan, M. Gell, Surf. Coat. Technol., 146-147 (2001) 70-78.

[22] P. Niranatlumpong, C.B. Ponton, H.E. Evans, Oxid. Met., 53 (2000) 241-258.

[23] P. Poza, P.S. Grant, Surf. Coat. Technol., 201 (2006) 2887-2896.

[24] D. Naumenko, V. Shemet, L. Singheiser, W. Quadakkers, J. Mater. Sci., 44 (2009) 1687-1703.

[25] T. Koomparkping, S. Damrongrat, P. Niranatlumpong, J. Therm. Spray Technol., 14 (2005) 264-267.

[26] P. Fox, G.J. Tatlock, Mater. Sci. Technol., 5 (1989) 816-827.

[27] N. Czech, F. Schmitz, W. Stamm, Surf. Coat. Technol., 68-69 (1994) 17-21.

[28] N. Czech, F. Schmitz, W. Stamm, Surf. Coat. Technol., 76-77 (1995) 28-33.

[29] C.E. Lowell, C.A. Barrett, R.W. Palmer, J.V. Auping, H.B. Probst, Oxid. Met., 36 (1991) 81-112.

[30] J.A. Nesbitt, Technical Report No. NASA/TM-2000-209271, (2000).

[31] E. Lee, D. Chartier, R. Biederman, R. Sisson, Surf. Coat. Technol., 32 (1987) 19-39.

[32] D.R.G. Achar, R. Munoz-Arroyo, L. Singheiser, W.J. Quadakkers, Surf. Coat. Technol., 187 (2004) 272-283.

[33] M.S.A. Karunaratne, S.L. Ogden, S.D. Kenny, R.C. Thomson, Mater. Sci. Technol., 25 (2009) 287-299.

[34] S.M. Meier, D.M. Nissley, K.D. Sheffler, Technical Report NASA Contractor Report 18911/NAS3-23944, (1991).

[35] R. Pillai, W.G. Sloof, A. Chyrkin, L. Singheiser, W.J. Quadakkers, Mater. High Temp., 32 (2015) 57-67.

[36] K. Yuan, R. Eriksson, R. Lin Peng, X.-H. Li, S. Johansson, Y.-D. Wang, Surf. Coat. Technol., 232 (2013) 204-215.

[37] R. Eriksson, K. Yuan, X.-H. Li, R. Lin Peng, Surf. Coat. Technol., 253 (2014) 27-37.

[38] K. Yuan, R. Lin Peng, X.-H. Li, S. Johansson, Y.-D. Wang, Surf. Coat. Technol., 261 (2015) 86-101.

[39] M.S.A. Karunaratne, I. Di Martino, S.L. Ogden, D.L. Oates, R.C. Thomson, Metallurgical and Materials Transactions A, 43 (2011) 774-788.

[40] K. Yuan, R. Eriksson, R. Lin Peng, X.-H. Li, S. Johansson, Y.-D. Wang, Surf. Coat. Technol., 254 (2014) 79-96.

[41] R. Eriksson, K. Yuan, X.-H. Li, R. Lin Peng, Surf. Coat. Technol., 253 (2014) 27-37.

[42] D. Whittle, D. Evans, D. Scully, G. Wood, Acta Metall., 15 (1967) 1421-1430.

[43] T. Hodgkiess, G.C. Wood, D.P. Whittle, B.D. Bastow, Oxid. Met., 12 (1978) 439-449.

[44] G. Wang, B. Gleeson, D.L. Douglass, Oxid. Met., 35 (1991) 317-332.

[45] F.H. Stott, Rep. Prog. Phys., 50 (1987) 861.

[46] G. Wahl, Thin Solid Films, 107 (1983) 417-426.

[47] P. Carter, B. Gleeson, D. Young, Acta Mater., 44 (1996) 4033-4038.

[48] F. Gesmundo, B. Gleeson, Oxid. Met., 44 (1995) 211-237.

[49] S. Saeidi, K.T. Voisey, D.G. McCartney, J. Therm. Spray Technol., 20 (2011) 1-13.

[50] L. Russo, M. Dorfman, Thermal Spraying: Current status and future trends., Osaka, Japan, (1995) 681-686.

[51] R. Syed, N. Sobh, U. Ravaioli, G. Popescu, M. Mohamed, imageJ, 2009.

[52] L. Lelait, S. Alpérine, R. Mévrel, J. Mater. Sci., 27 (1992) 5-12.

[53] J. Andersson, T. Helander, L. Höglund, P. Shi, B. Sundman, Calphad, 26 (2002) 273-312.

[54] A. Borgenstam, L. Höglund, J. Ågren, A. Engström, J. Phase Equilib., 21 (2000) 269-280.

[55] N. Saunders, Superalloys 1996. TMS, Warrendale, PA, 115 (1996).

[56] Z. Hashin, S. Shtrikman, J. Appl. Phys., 33 (1962) 3125-3131.

[57] T. Gómez-Acebo, B. Navarcorena, F. Castro, J Phs Eqil and Diff, 25 (2004) 237-251.

[58] D. Seo, K. Ogawa, T. Shoji, S. Murata, J. Therm. Spray Technol., 17 (2008) 136-143.

[59] A. Gil, D. Naumenko, R. Vassen, J. Toscano, M. Subanovic, L. Singheiser, W.J. Quadakkers, Surf. Coat. Technol., 204 (2009) 531-538.

[60] C. Wagner, J. Electrochem. Soc., 99 (1952) 369-380.

[61] D.A. Porter, K.E. Easterling, Phase transformations in metals and alloys, CRC press, London, 1992.

Table 1

Relationship between initial assumed oxide thickness, the time for the corresponding oxide to grow, the resultant initial β depletion zone, and the initial Al flux at each initial oxide thickness.

Initial oxide thickness (μm)	Time for the initial oxide to grow (s)	Initial β depletion zone (μm)	Initial Al flux (mol/(m²s))
0.25	100	1.4	6.46×10^{-5}
0.5	800	2.8	1.61×10^{-5}
1	6441	5.6	4.00×10^{-6}

Table 2

Comparison of γ and β phase compositions of CoNiCrAlY (Co-31.7Ni-20.8Cr-8.1Al-0.5Y, all in wt%, neglecting Y) calculated from Thermo-Calc using the TTNi7 database at 1100 °C and experimentally measured by EDX following the initial vacuum heat treatment for 2 h at 1100 °C.

Element			γ phase		β phase	
			wt%	at%	wt%	at%
Calculated TTNi7 (at 1100 °C)		Co	43.0	39.4	28.6	23.2
		Ni	27.4	25.2	44.8	36.6
		Cr	24.9	25.9	8.4	7.7
		Al	4.8	9.5	18.3	32.4
Experimental EDX results		Co	41.1 ± 0.5	38.0 ± 0.5	24.6 ± 0.5	20.0 ± 0.5
		Ni	29.2 ± 0.5	27.1 ± 0.4	48.2 ± 1.2	39.3 ± 0.9
		Cr	25.8 ± 0.2	27.0 ± 0.3	8.7 ± 1.1	8.0 ± 1.1
		Al	3.8 ± 0.2	7.8 ± 0.4	18.5 ± 0.4	32.8 ± 0.6

Table 3

Comparison of γ and β phase fractions between experimental measurements and calculated values using Thermo-Calc with the TTNi7 database at 1100 °C

	Phase mass fraction		Phase volume fraction	
	γ	β	γ	β
TTNi7 Calculated	75%	25%	72%	28%
Experimental measurements	-----	-----	69 ± 2%	30 ± 2%

FIGURES
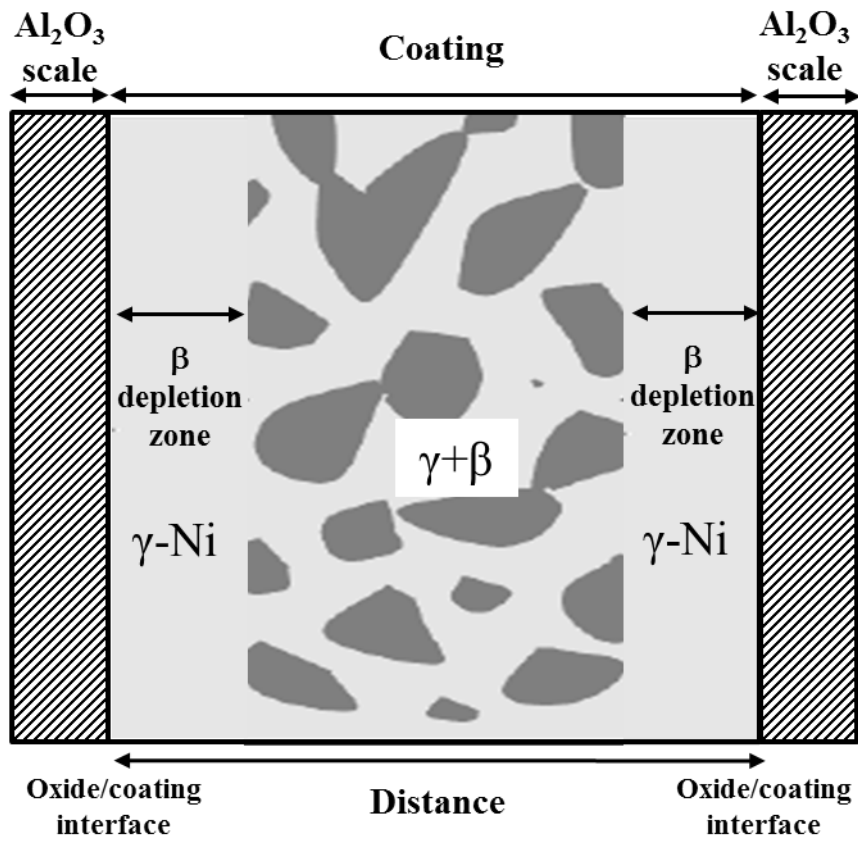
Fig. 1 A schematic cross section of a free-standing MCrAlY coating showing the development of β depletion zone during oxidation.
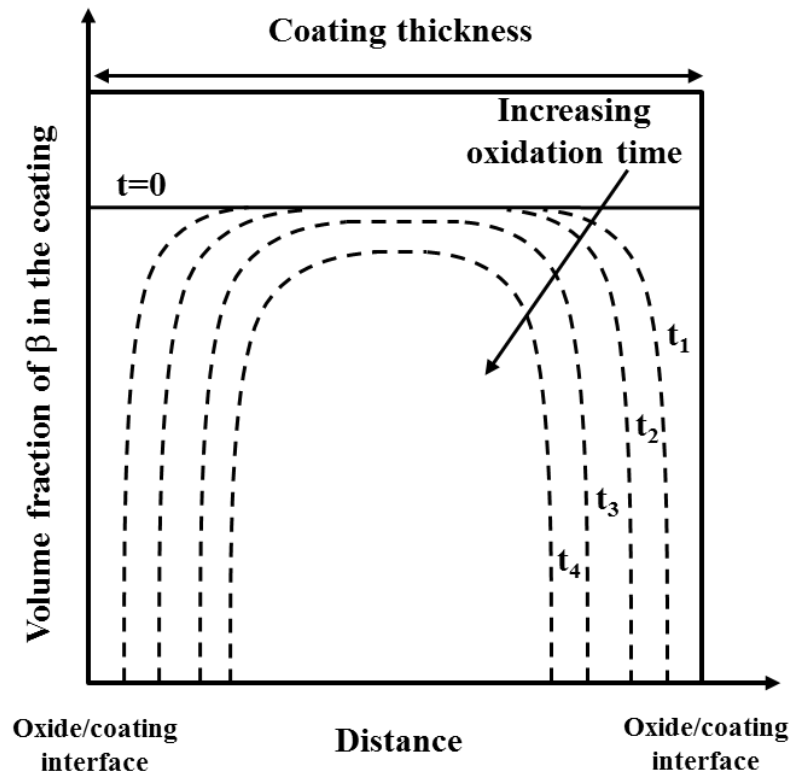
Fig. 2 A schematic diagram showing the expected development of β volume fraction (dotted line) in the free-standing coating with increasing oxidation time (t_1, t_2, t_3, t_4). The solid line (t=0) shows the initial β fraction.
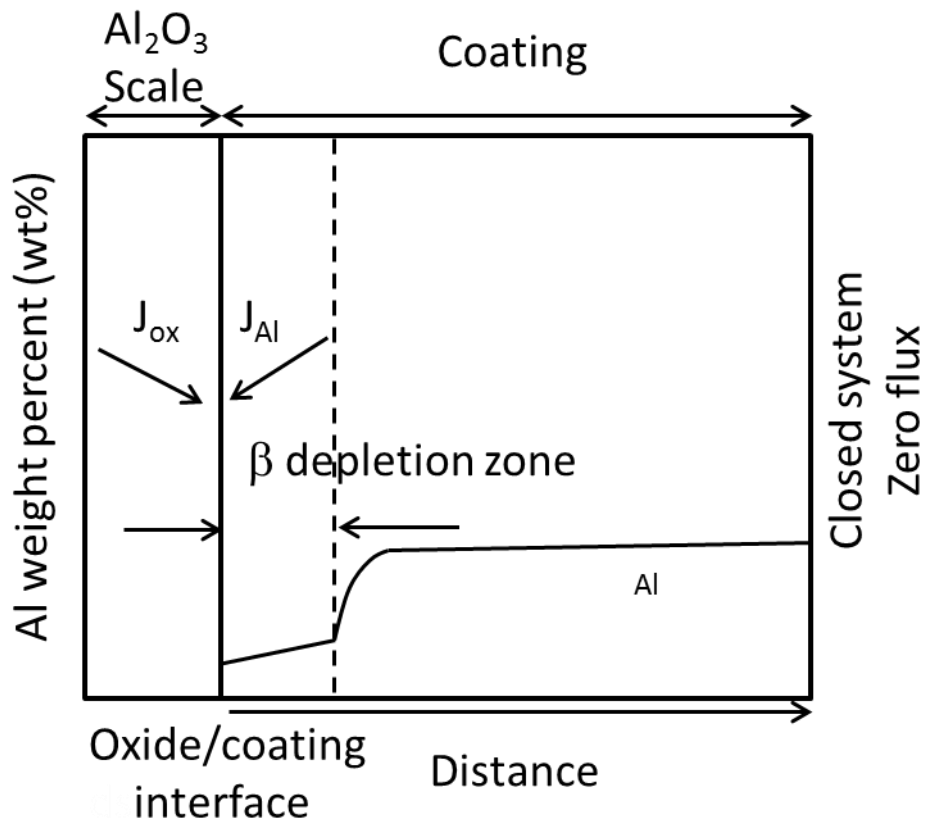
Fig. 3 A diagram showing schematically the variation of Al concentration against distance with an Al flux, J_{Al}, in the coating towards the oxide/coating interface to meet the oxygen flux, J_{ox}, to form the Al_2O_3 scale, and the formation of a β depletion zone.
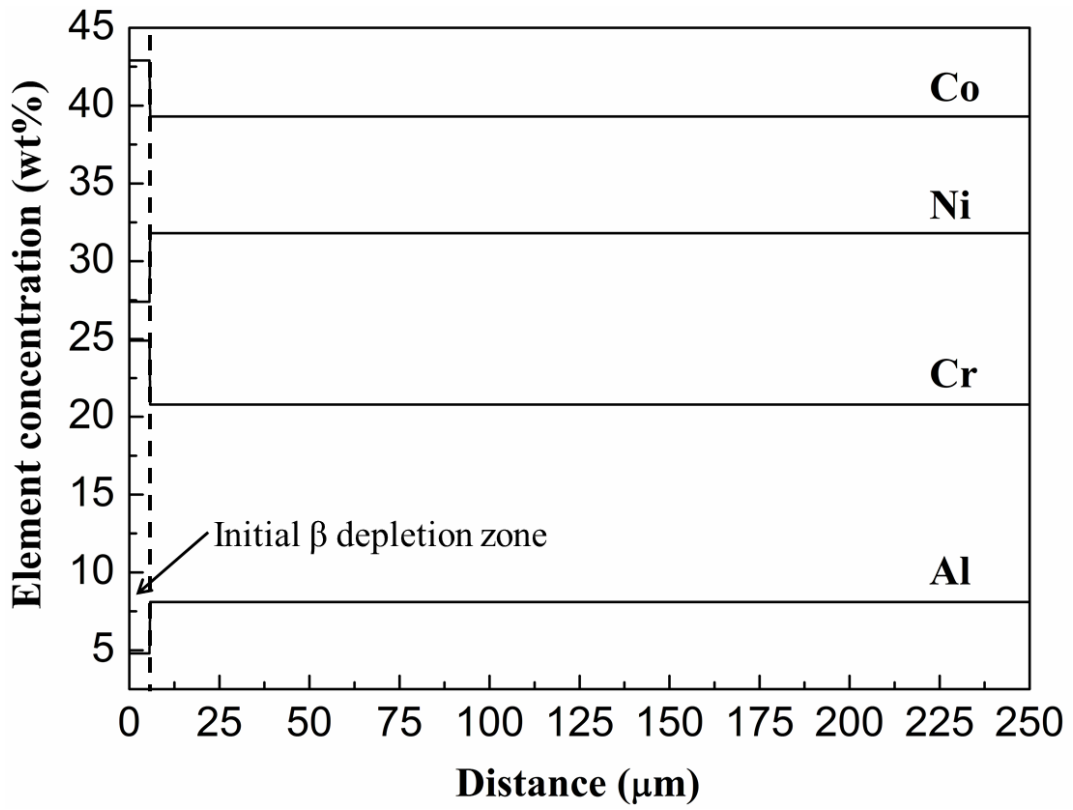
Fig. 4 Plot of the initial element profile when an initial oxide thickness of 1 μm is assumed. The initial β depletion zone is 5.6 μm. The composition in the β depletion zone is referred as the γ phase composition and the composition in the γ+β region is referred as the initial alloy composition.
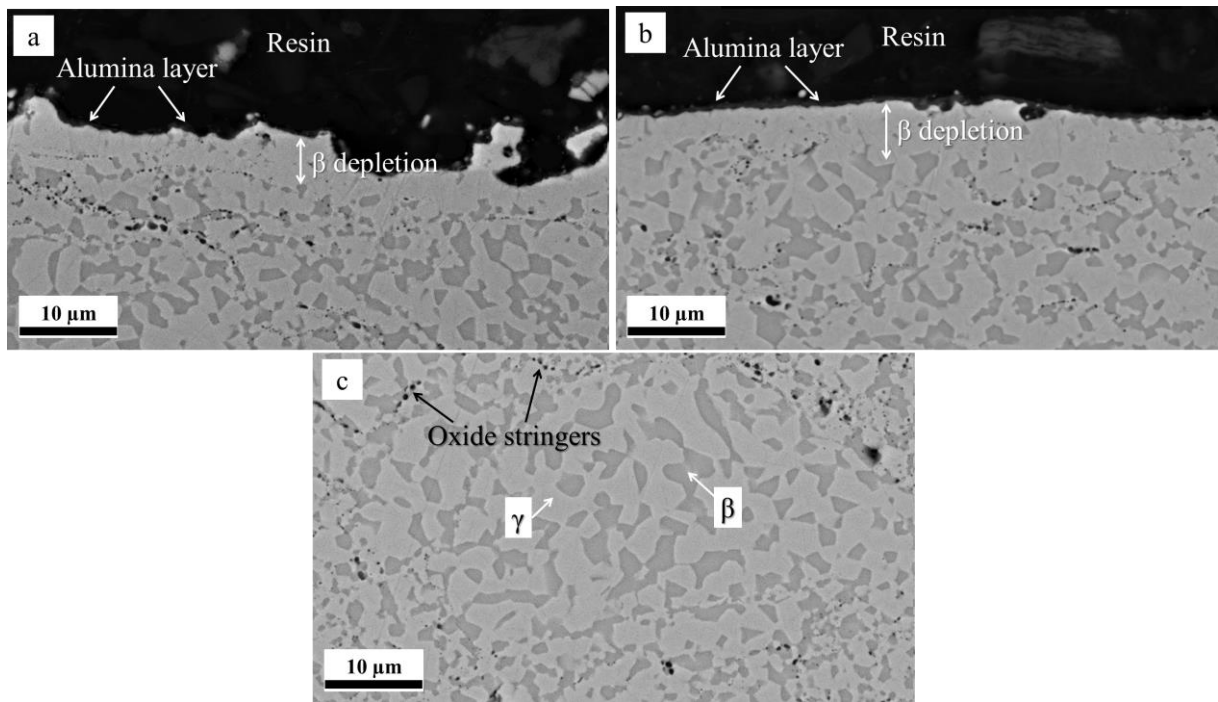
Fig. 5 BSE micrographs of the HVOF sprayed CoNiCrAlY bond coat following vacuum heat treatment: (a) rough surface; (b) polished surface; (c) general microstructure of the coating showing the γ+β structure with some oxide stringers embedded in the coating.
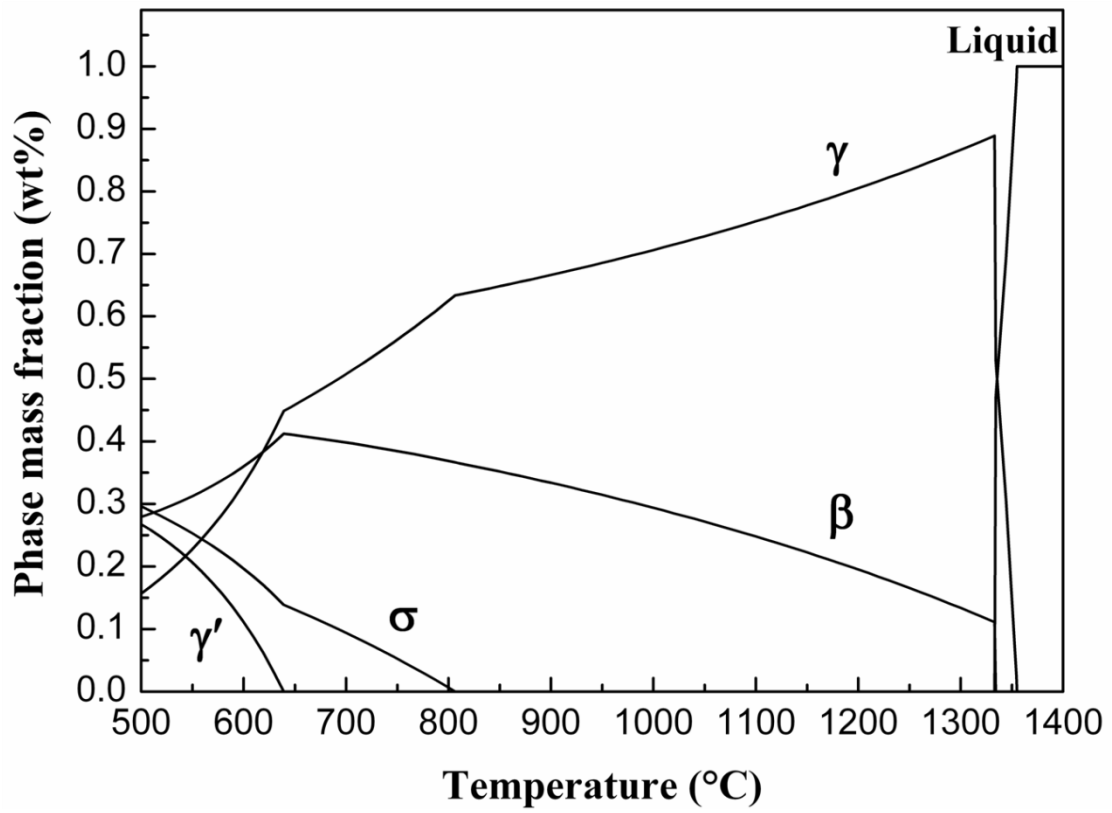
Fig. 6 Phase mass fraction map of CoNiCrAlY (Co-31.7Ni-20.8Cr-8.1Al-0.5Y, all in wt%, neglecting Y) obtained from Thermo-Calc using TTNi7 database.
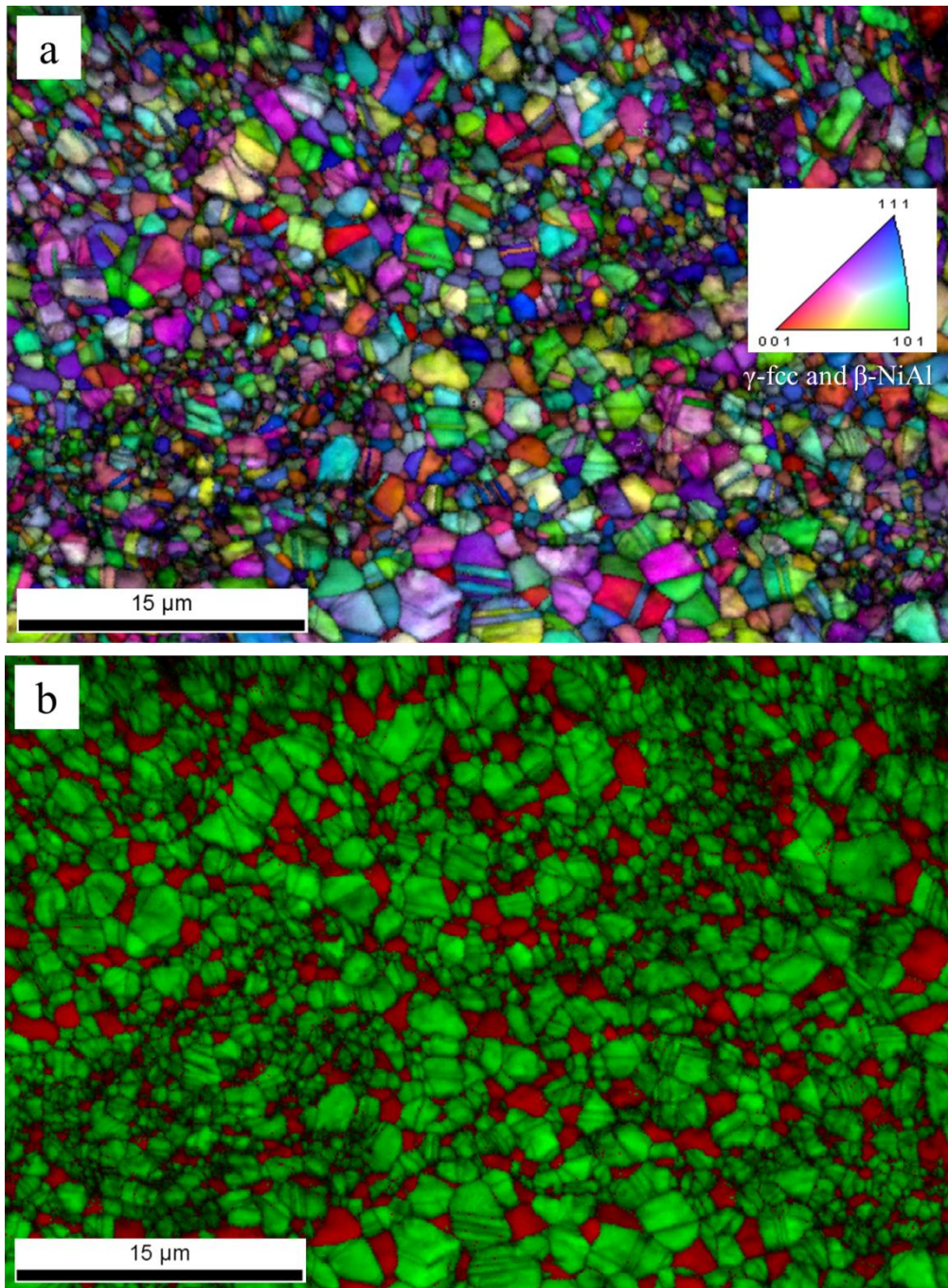
Fig. 7 EBSD map showing the grain structure of the CoNiCrAlY coating: (a) inverse pole figure map showing the grain orientations; (b) corresponding phase map indicating the individual γ and β grains (γ in green and β in red). (For interpretation of the references to colour in this figure legend, the reader is referred to the web version of this article.)
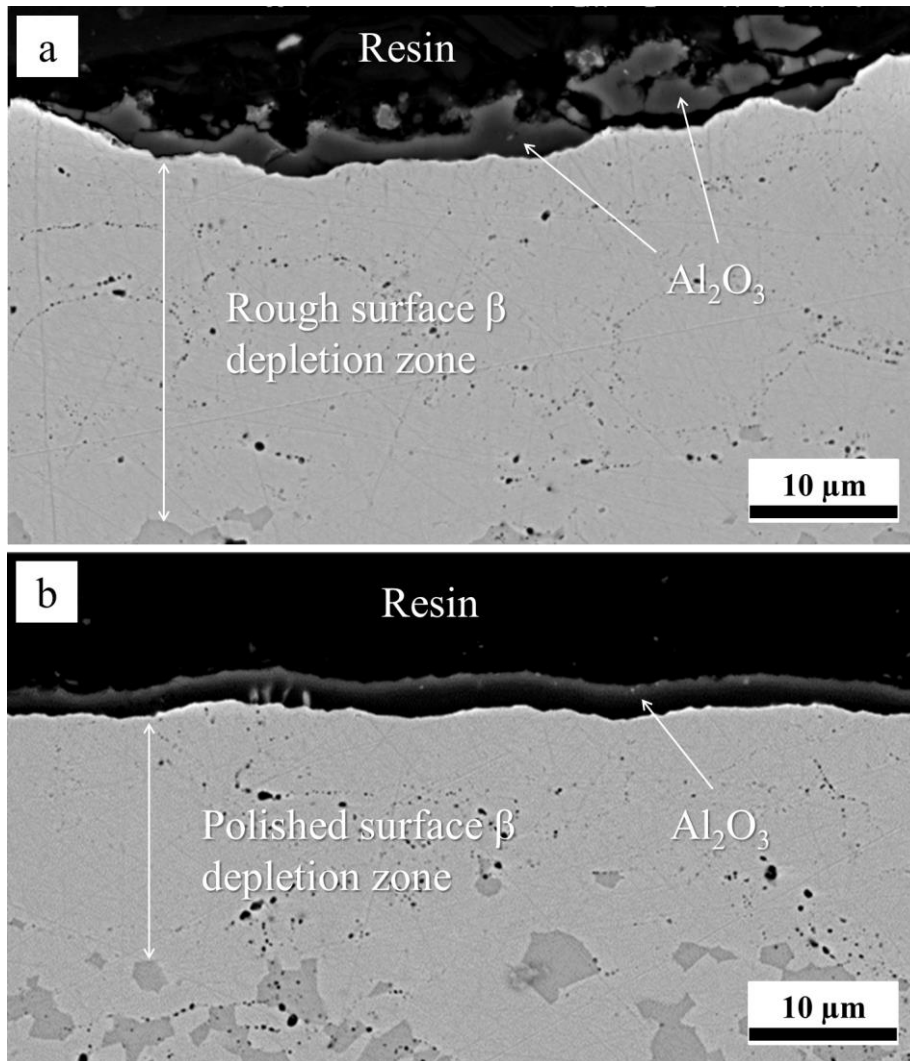
Fig. 8 Oxidation and β depletion of the CoNiCrAlY coating after oxidation for 250 h at 1100 ℃: (a) rough oxidising surface; (b) polished oxidising surface.
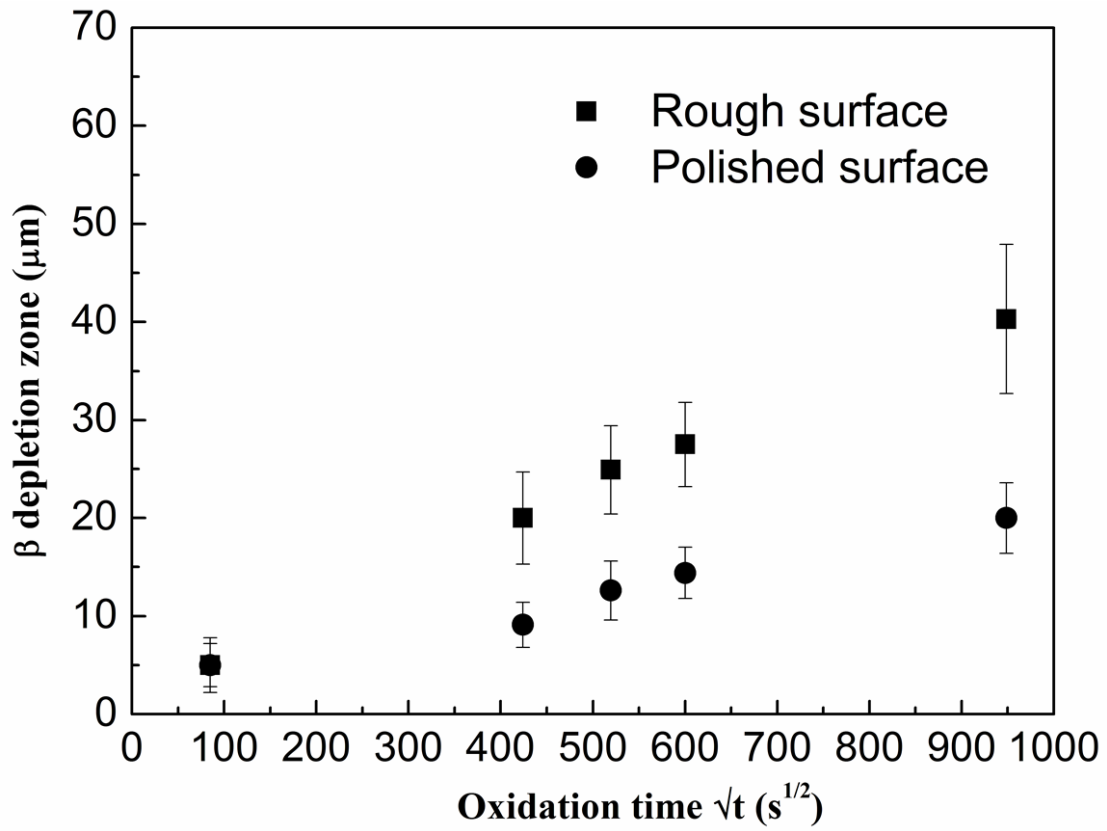
Fig. 9 β depletion zone measurements of free-standing CoNiCrAlY coating with rough and polished surfaces after oxidation at 1100 ℃ for 50, 75, 100 and 250 h. The initial β depletion zone formed after the initial heat treatment at 1100 ℃ for 2 h is also included. Error bars represent the standard deviation of measurements.
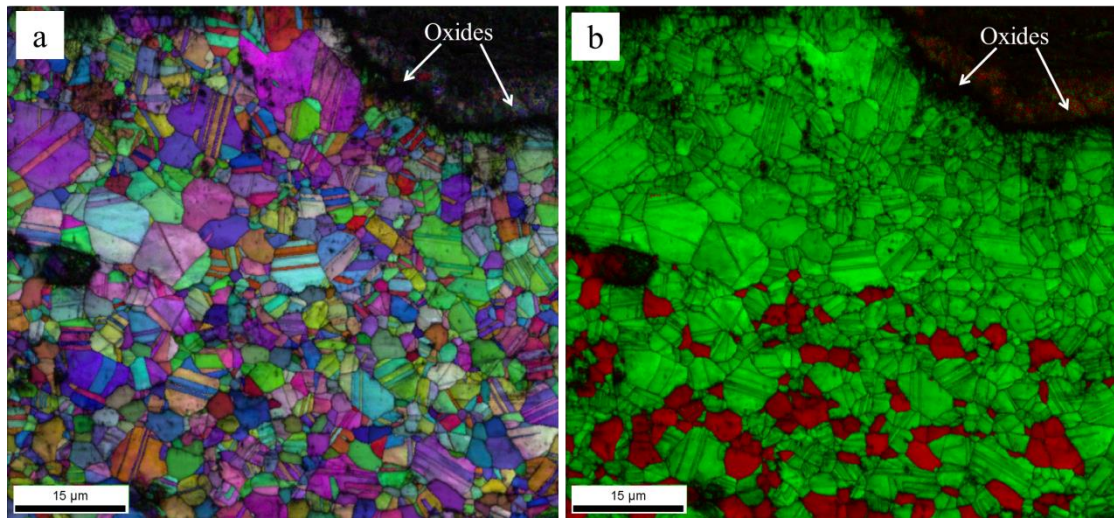
Fig. 10 EBSD mapping showing an increase of the γ grain size in the β depletion zone at the rough surface of the CoNiCrAlY coating after oxidation for 250 h at 1100 ºC: (a) inverse pole figure map showing the grain orientations; (b) corresponding phase map indicating the individual γ and β grains (γ in green and β in red). (For interpretation of the references to colour in this figure legend, the reader is referred to the web version of this article.)
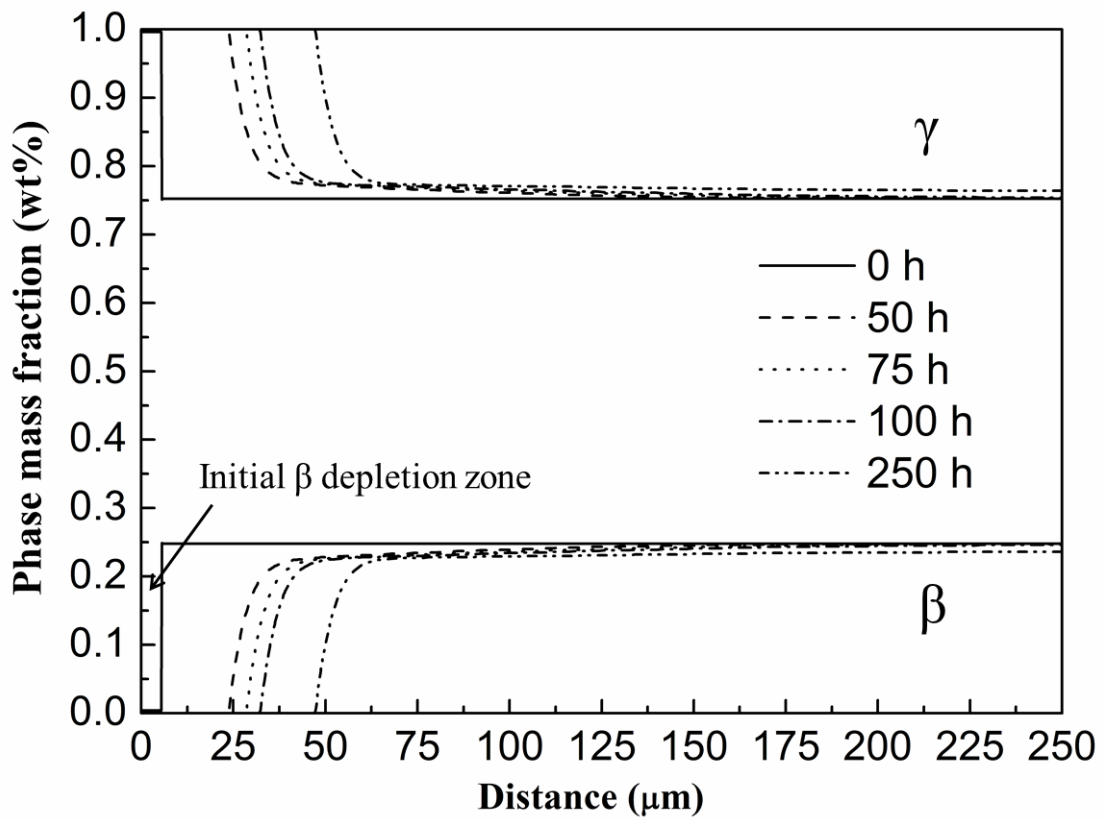
Fig. 11 Plots of phase mass fraction versus distance from the surface obtained from DICTRA calculation. Data are plotted for 4 different oxidation times.
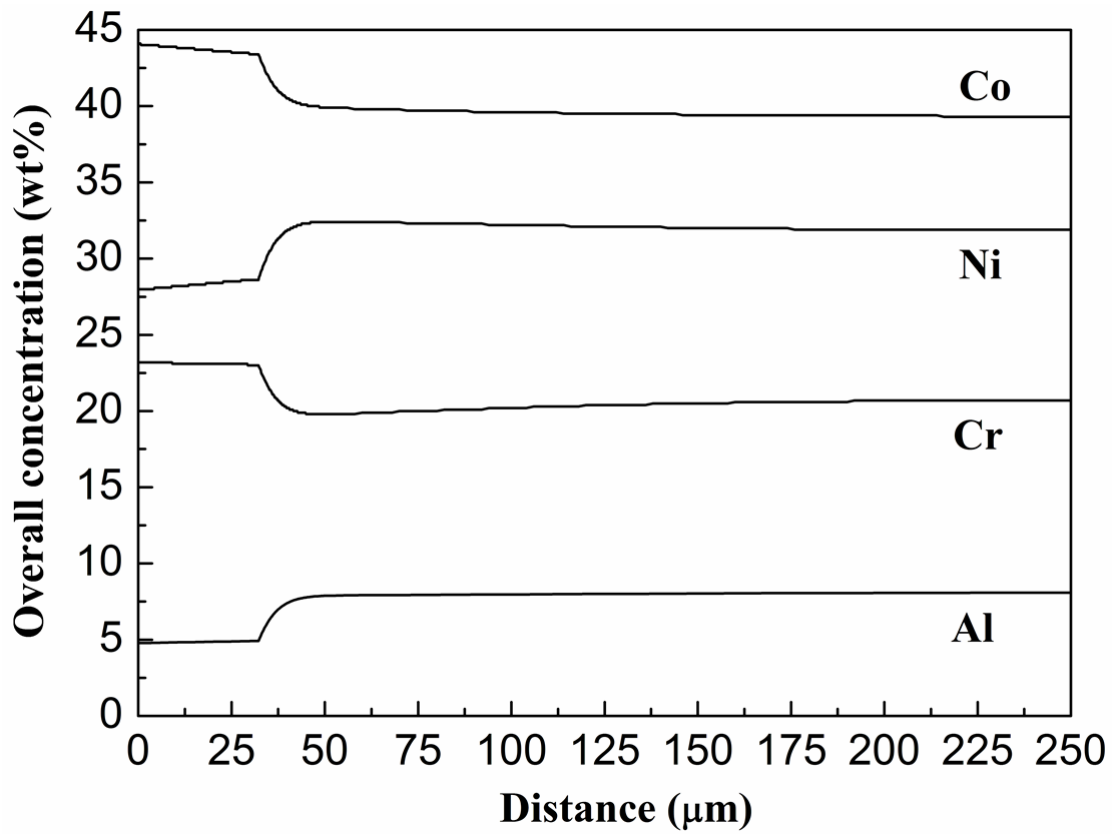
Fig. 12 Plots of element concentration versus distance from the oxidising surface after 100 h diffusion calculations. The β depletion zone extends up to ~35 μm into the sample. In the two-phase region, compositions are the average of the two phases.
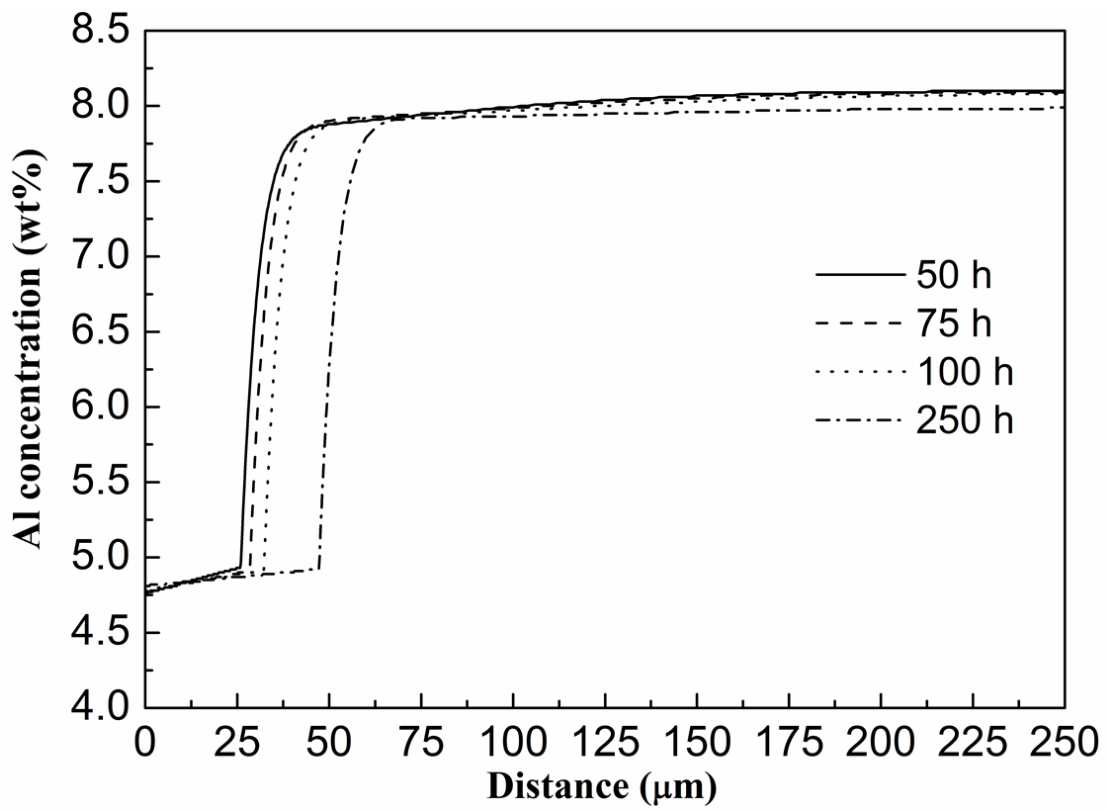
Fig. 13 Plot of Al concentration versus distance for different times at 1100 ℃, showing the Al content near the oxide/coating interface is close to 4.8 wt%.
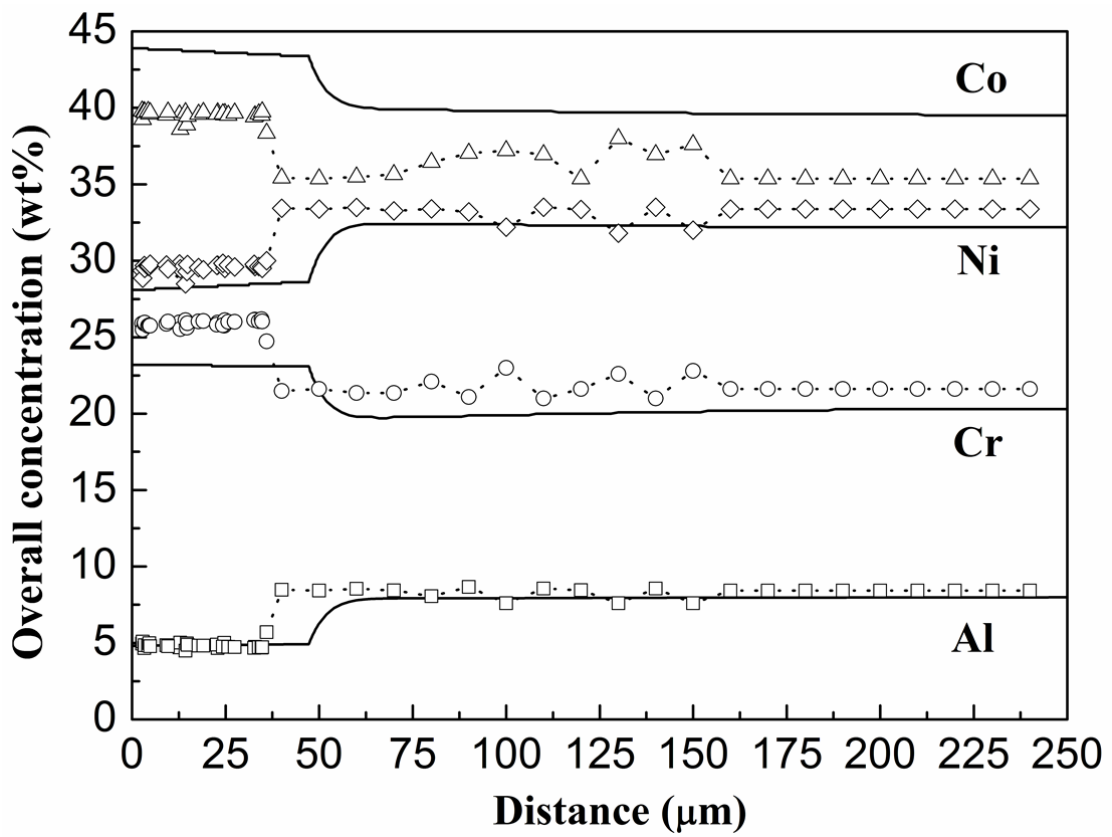
Fig. 14 Comparison of experimentally measured elemental profiles and modelling results at 1100 ℃ for 250 h, the solid lines are the modelling results and the dotted-symbol lines are the EDX measurements.
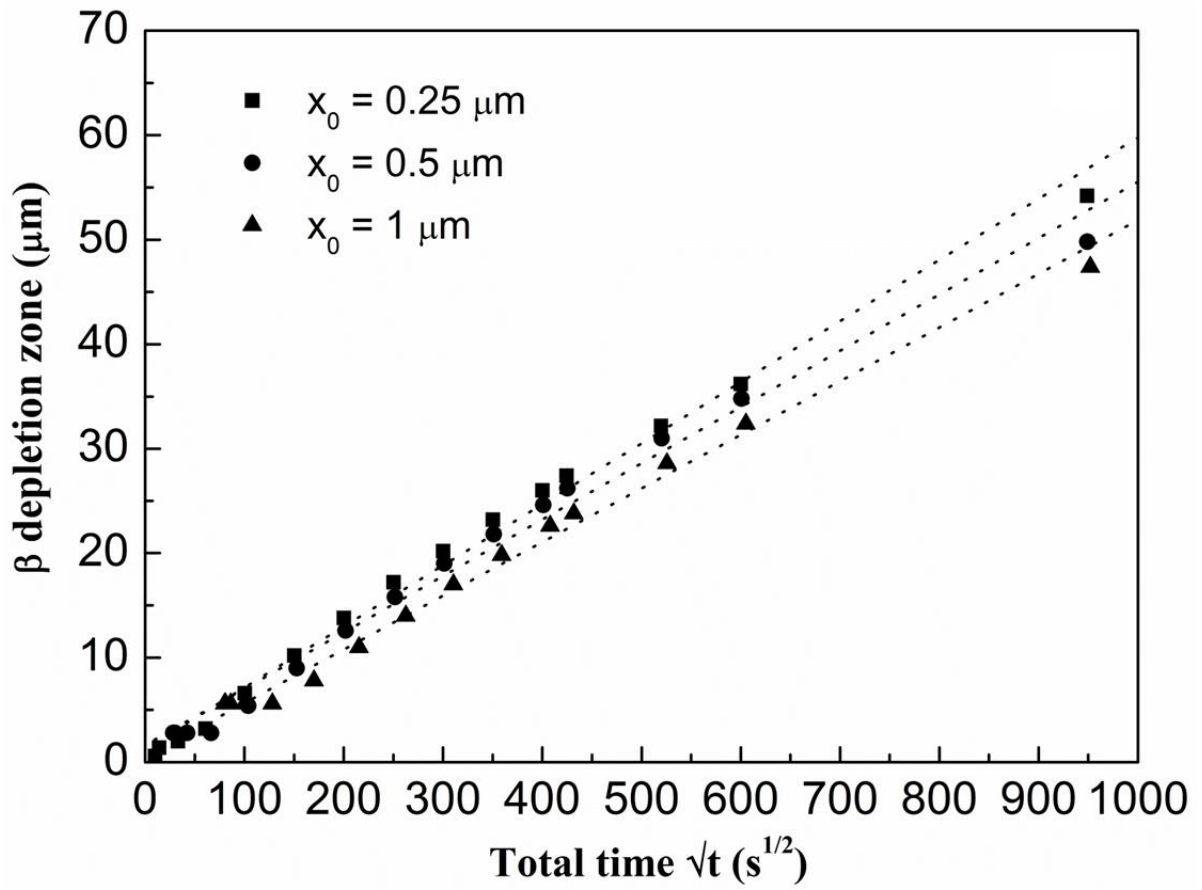
Fig. 15 Plot of β depletion zone versus $\sqrt{t}$ for three different initial oxide thicknesses (1100 °C exposure).
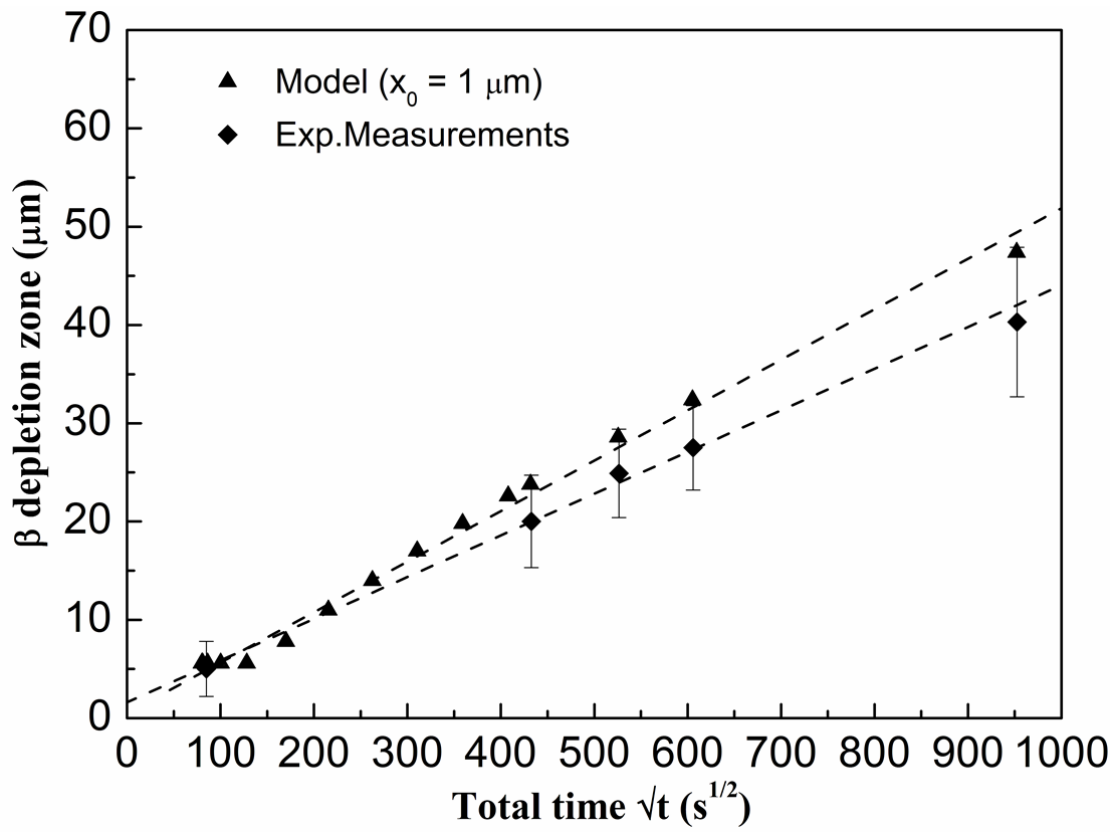
Fig. 16 Plots of β depletion zone thickness versus $\sqrt{t}$ from experimental measurements and predicted from the DICTRA model. An initial oxide thickness of 1 μm is assumed and the temperature is 1100 ºC
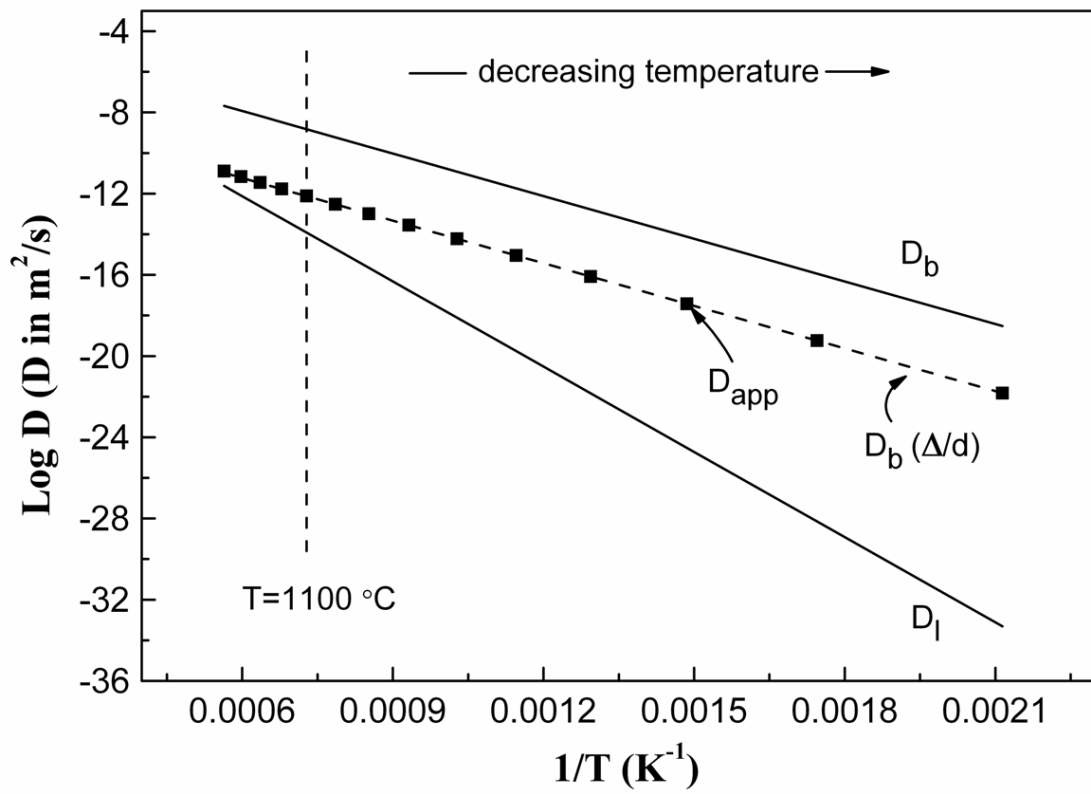
Fig. 17 Plot of log D versus 1/T for the lattice diffusion coefficient [33] and grain boundary diffusion coefficient (Eq. 12).